ACS APPLIED MATERIALS & INTERFACES

Research Article

www.acsami.org

Morphology-Driven High-Performance Polymeric Photodetector

Dae Sung Chung,*[,†] Yecheol Rho,[‡] Moonhor Ree,*[,‡] Soon-Ki Kwon,[§] and Yun-Hi Kim*[,⊥]

[†]Department of Chemical Engineering, Dong-A University, Busan, 604-714, Korea,

[‡]Department of Chemistry, Division of Advanced Materials Science, Center for Electro-Photo Behaviors in Advanced Mole-cular Systems, BK School of Molecular Science, and Polymer Research Institute, POSTECH, Pohang, 790-784, Korea,

[§]School of Nano & Advanced Materials Science and Engineering and ERI, and [⊥]Department of Chemistry and Research Institute of Natural Science (RINS), Gyeongsang National University, Jinju 660-701, Korea

ABSTRACT: The influence of polymer/fullerene morphology on photodetector performance is reported. Various morphologies of spin-coated films are generated by different blending ratio. Morphological study combined with measurement of charge carrier mobility reveals that blend films with an excess content of crystalline fullerene have a phase-separated morphology, resulting in enhanced charge carrier mobility. Under this phase separated morphology, photovoltaic performance is enhanced because of the generation of percolating pathways for charge carriers. Interestingly, however, a homogeneous morphology is found to be more beneficial for photodetector application than this phase separated morphology. An optimized device displayed 3 dB bandwidth up to 1 kHz and detectivities up to $D = 1.1 \times 10^{10}$ cm $Hz^{1/2}$ W^{-1}. These results emphasize the importance of developing an independent strategy for designing high performance photodetectors separately from solar cell devices both in terms of materials and device geometry. Possible relations between morphology and various figures of merit of photodetectors are discussed.

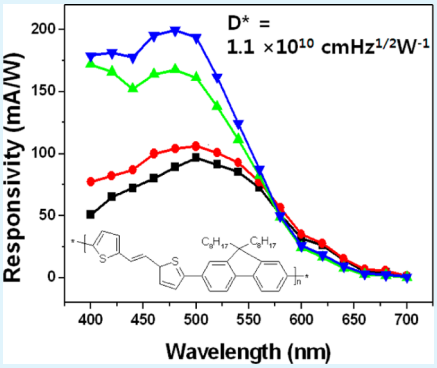

KEYWORDS: *photodetector, polymer, semiconductor, detectivity, mobility*

INTRODUCTION

As demand for renewable energy sources grows, photovoltaic energy conversion has attracted increasing attention. Organic materials present the most cost-effective approach to fabricating solar cells, because of their potential in realizing flexible lightweight large-area devices.[1−5] Polymer solar cells (PSCs) based on conjugated polymers and soluble fullerene blends are particularly attractive because of their ease of processing and mechanical flexibility.[6−18] Their material properties can be easily tailored by modifying the chemical composition of the components, allowing for greater customization than is possible using traditional inorganic solar cells.[19] In addition, these advantages enable their applications as the active layer of polymer photodetectors (PPDs), which have a similar working mechanism as that of solar cells. Motivated by these advantages, significant progress has been made in PSC and PPD technology. The early type devices were mainly fabricated using MEH-PPV and yielded power conversion efficiency (PCE) of around 2% in the case of PSCs[20] and responsivity of 0.2 A/W for PPDs,[21] respectively. Optimization of poly(3-hexylthiophene) (P3HT), which has been the main focus of PSC and PPD research, has yielded PCEs that exceed 5%[22] and responsivity higher than 50 A/W,[23] respectively. In this case, unusually high responsivity of PPDs could be achieved by adding CdTe nanoparticles to a photoactive P3HT:PCBM blend. More recently, another successful polymer, poly[2,6-(4,4,-bis-(2-ethylhexyl)-4H-cyclopenta[2,1-b;3,4-b′]-dithiophene)-alt-4,7-(2,1,3-benzothiadiazole)] (PCPDTBT), also enabled PCEs of PSCs higher than 5%[24] as well as responsivity of PPDs higher than 0.3 A/W.[25]

Two synthetic strategies have been widely adopted toward the development of photoactive polymeric semiconductors: (i) reducing the bandgap for better light harvesting, and (ii) lowering the highest occupied molecular orbital (HOMO) energy level to increase the open circuit voltage (V_{OC}) of the solar cell, which is empirically proportional to the difference between the HOMO of the electron donor and the LUMO of the electron acceptor. Note that this expression is a simplified empirical expression without physical consideration. Actually, V_{OC} is not independent variable on the charge carrier recombination rate, light intensity, energy of charge transfer states, and the degree of crystalline order of donor−acceptor materials.[26] In terms of morphology, it was found that conjugated polymers and fullerene molecules should be intermixed to achieve efficient exciton dissociation at the large interfacial area.[9] At the same time, there also should be continuous pathways for the transport of separated charge carriers, and thus film thickness does not have to be sacrificed to maximize light absorbing ability. Because general polymer-fullerene systems do not show such an optimized morphology

Received: June 21, 2012
Accepted: August 10, 2012
Published: August 10, 2012

   dx.doi.org/10.1021/am301128d | ACS Appl. Mater. Interfaces 2012, 4, 4758−4763

without any post-treatment, various postoptimization processes have been studied with many material systems.[4]

As described above, synthetic and morphological methodologies to optimize PSCs have been studied extensively. However, it is not clear whether the developed approaches would also work well for PPD applications. One of the major differences between application of PSCs and PPDs is the impact of the photon to electron conversion response speed. In the case of PSCs, long-lived photocharge carriers can help balanced hole−electron extraction in the bulk heterojunction (BHJ) film by reducing the probability of unnecessary hole−electron recombination. However, for photodetector application, especially for imaging systems, these long-lived photocharge carriers can often introduce overlap between each imaging frame. In general, a temporal response in the range of tens of milliseconds is necessary for lag-free imaging application.[27−30] This suggests that morphological and/or chemical requirements for PSCs and PPDs may be different.

With these considerations, in this study, we attempted to develop a morphology-based methodology for optimizing PSCs and PPDs independently. To this end, we have introduced a novel low crystalline polymeric semiconductor, poly[(1,2-bis-(2′-thienyl)vinyl-5′,5″-diyl)-alt-(9,9-dioctyldecylfluorene-2,7-diyl] (PTVTF). PTVTF was found to have a considerably amorphous structure from synchrotron-generated X-ray diffraction and absorption experiments.[31] It consequently has a very stable and reproducible morphology while maintaining relatively good electrical characteristics. These properties enabled experiments aimed at comparing the electrical performance of the polymer/fullerene blend as PSCs and PPDs as well as their morphology and structures using the same film or device. [6,6]-phenyl C_{71} butyric acid methyl ester ($PC_{70}BM$) was employed to study the effects of fullerene contents on the final morphology, and thus their final device performance as either PSCs or PPDs.

EXPERIMENTAL SECTION

Preparation of Materials. *Synthesis of PTVTF.* 1,2-(E)-Bis(5′-bromo-2′-thienyl)ethene was prepared from 2-bromothiophene via a Wittig reaction in a yield of approximately 58%. The Suzuki coupling reaction was employed in the polymerization of PTVTF. After polymerization, end-capping was carried out with 2-bromonaphthalene. The Soxhlet extraction of the crude polymer to remove oligomeric materials afforded PTVTF an orange color in a yield of 60%. The structure of the obtained PTVTF was confirmed with ^{1}H NMR, ^{13}C NMR, and IR spectroscopy.

Other materials were purchased from commercial sources (Aldrich and Nanobest) and used without further purification.

Device Fabrication. After cleaning the prepatterned ITO-coated glass, PEDOT:PSS (Baytron P TP AI 4083, Bayer AG) was spin-coated to a thickness of 30−50 nm and annealed at 120 °C (for 60 min) in air. The active layer was spin-coated onto the PEDOT:PSS layer for 60 s to a thickness of 100 nm. Finally, lithium fluoride (LiF) (1 nm)/Al (100 nm) cathodes were thermally deposited. The current density−voltage (J−V) characteristics were measured using Keithley 4200 source/measure units under either AM 1.5 G solar illumination (Oriel 1 kW solar simulator) with respect to the reference cell PVM 132 (calibrated at the National Renewable Energy Laboratory, NREL, at an intensity of 100 mW/cm^2). or the monochromatic light from a 150 W xenon arc lamp assembled with a 1/8°m monochromator. To measure the photocurrent spectra, we synchronized the monochromator with the source meter and mechanical chopper with 10 Hz.

Characterization. UV−vis measurements were carried out on a UV−vis-NIR spectrophotometer (Cary 5000: Varian Co. and FR 6500, JASCO CO.). Cyclic voltammetry measurements of the polymer and fullerene films were performed on a BAS 100 B/W electrochemical analyzer in acetonitrile, with 0.1 M tetrabutylammonium perchlorate (Bu_4NClO_4) as the supporting electrolyte, at a scan rate of 100 mV/s. The potentials were measured against an Ag/AgCl reference electrode with ferrocene as the internal standard. The onset potentials were determined from the intersection of the tangents to the rising current and to the background current of the cyclic voltammogram. GIXS measurements were carried out at the 4C1 and 4C2 beamlines of the Pohang Accelerator Laboratory.[32] The samples were measured at a sample-to-detector distance (SDD) of 131 mm. Data were typically collected for 60 s using an X-ray radiation source of λ = 0.138 nm with a two-dimensional charge-coupled detector (2D CCD: Roper Scientific, Trenton, NJ, USA). Samples were mounted on a home-built z-axis goniometer equipped with a vacuum chamber. The incident angle α_i of the X-ray beam was set to 0.16°, an intermediate value between the critical angles of the films and the silicon substrate ($\alpha_{c,f}$ and $\alpha_{c,s}$). Scattering angles were corrected according to the positions of the X-ray beams reflected from the silicon substrate interface as a function of incident angle α_i and with respect to a precalibrated silver behenate (TCI, Japan) powder. Aluminum foil pieces were employed as semitransparent beam stops, because the intensity of the specular reflection from the substrate was much stronger than the intensity of GIXS near the critical angle. TEM images were obtained using a HITACHI-7600 operated at 100 kV.

RESULTS AND DISCUSSION

The chemical structure of PTVTF and its thin film absorption spectra are introduced in Figure 1. The UV−vis absorption

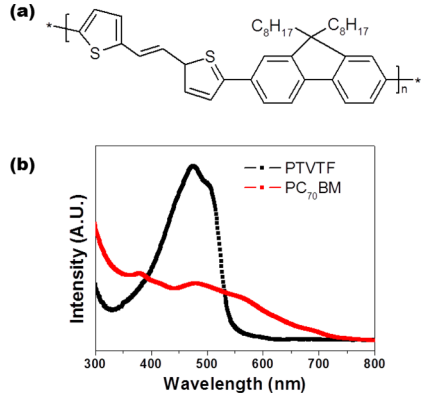

Figure 1. (a) Chemical structure of PTVTF, (b) UV−vis absorption spectra of polymer and PC70BM (thin film absorption spectra).

spectra of PTVTF revealed nearly identical solution and film state absorption, spanning the range of 400−550 nm, and were unaffected by thermal annealing, consistent with the film's amorphous character. Although fullerene derivatives generally have a limited absorption cross-section in the visible range, $PC_{70}BM$ was shown to absorb more strongly in the visible region than did other fullerenes. The reduced symmetry of $PC_{70}BM$ permits transitions that are forbidden in the highly symmetric $PC_{60}BM$, which increased the intensity and breadth of the absorption spectrum. The HOMO and LUMO levels were measured by cyclic voltammetry and the optical bandgap, yielding values of 5.3 and 2.9 eV, respectively. The difference between the LUMO of PTVTF and that of $PC_{70}BM$ is ∼0.8 eV, which can drive photoinduced charge separation in those blend films.

To determine the morphological characteristics that will yield optimized devices, we fabricated PTVTF/$PC_{70}BM$ BHJ devices with various blending ratios. The polymer and fullerenes were blended in weight ratios of 2:1, 1:1, 1:2, and 1:4 (giving fullerene weight content of 33, 50, 67, and 80%, respectively) in

dx.doi.org/10.1021/am301128d | ACS Appl. Mater. Interfaces 2012, 4, 4758−4763

dichlorobenzene. The morphologies of each blend were characterized by tapping mode Atomic Force Microscopy (AFM), as shown in Figure 2. Almost featureless amorphous

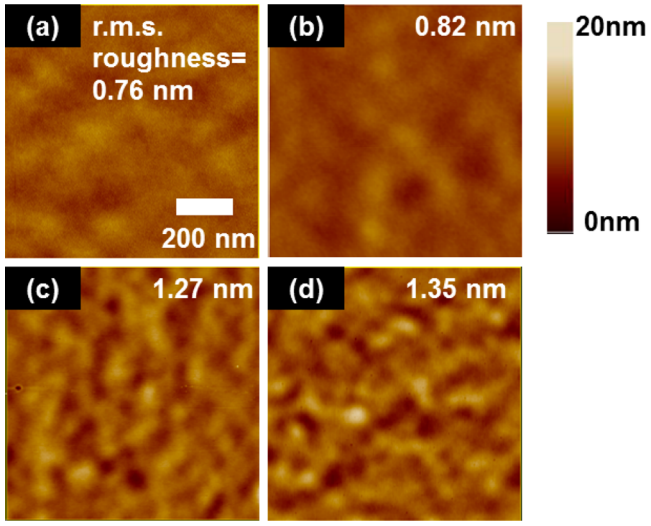

Figure 2. AFM images of PTVTF films blended with PC70BM in dichlorobenzene; the fullerene content is (a) 33, (b) 50, (c) 67, and (d) 80%.

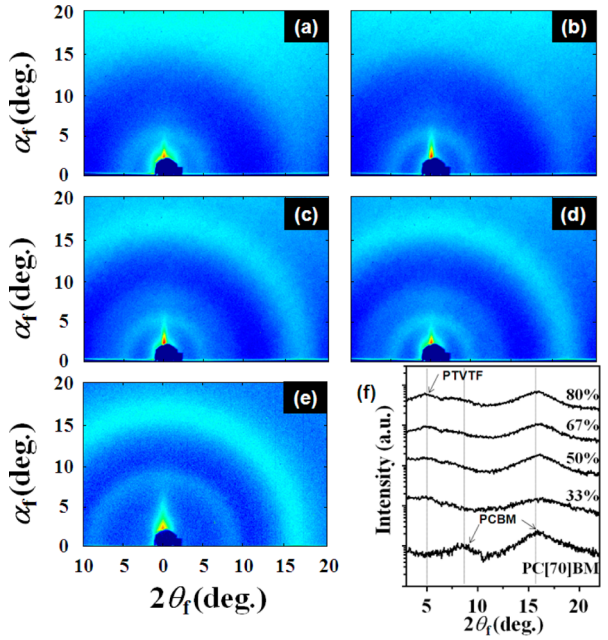

Figure 3. (a–d) GIXD images of PTVTF/PC70BM PSC thin films with various blend ratios and (e) homo- PC70BM. (f) Cross-sectional images of the GIXD patterns shown in (a–e) clearly show the variations in peak intensity.

morphology is observed in films with low fullerene contents, (Figure 2a, b), whereas clearly phase separated morphology is generated in films with high fullerene contents. (Figure 2c, d) Increase of rms roughness is also observed as denoted in the figure. In other words, the PTVTF/$PC_{70}BM$ blend morphology shows a phase transition between homogeneous and phase-separated morphologies at fullerene content between 50 and 67 wt %. Note that a continuous network formed by nanoscale (10–20 nm) phase separated domains is generally accepted as an ideal morphology for high-performance BHJ cells.[9]

To further analyze the formation of phase separation in the films of the PTVTF/$PC_{70}BM$ blend, a two-dimensional (2D) grazing incidence wide-angle X-ray scattering (GIWAXS) analysis was performed on the PTVTF/$PC_{70}BM$ blend films. Figure 3a–e show 2D GIWAXS patterns measured for various blend conditions of PTVTF/$PC_{70}BM$ blend thin films deposited onto PEDOT:PSS/ITO/glass substrates. Figure 3f shows the in-plane scattering profiles extracted from the scattering patterns shown in Figure 3 along the $2\theta_f$ direction at $2\alpha_f = 0.16°$. First, we obtained the GIWAXS patterns of a pristine $PC_{70}BM$ thin film with two isotropic scattering rings at $2\theta_f = 8.4°$ (d-spacing = 0.94 nm) and $2\theta_f = 16.02°$ (d-spacing = 0.50 nm), as provided in panels e and f in Figure 3. These two broad scattering rings were characteristics of randomly oriented $PC_{70}BM$ on the substrate. The inner isotropic scattering ring, with a d-spacing of 0.94 nm, is attributed to the mean interdistance between C_{70}-fullerene moieties, which show regular packing according to the molecular size of $PC_{70}BM$ without a specific packing direction on the thin film. The outer isotropic scattering ring, with a d-spacing of 0.50 nm, is attributed to the mean distance between some parts of one molecule and some parts of its adjacent molecule, not specific molecular packing, such as between the C_{70}-fullerene moiety of a $PC_{70}BM$ molecule and the adjacent tail component of the other $PC_{70}BM$ molecules. From the above results, $PC_{70}BM$ on the thin film does not have crystalline domains and is stacked loosely. As can be seen in Figure 3a, b, and f, the GIWAXS patterns of the blends containing 33 and 50% fullerene content revealed two broad weak isotropic scattering rings at $2\theta_f = 5.15°$ (d-spacing = 1.54 nm) and $2\theta_f = 16.02°$ (d-spacing = 0.50 nm). The inner isotropic ring corresponds to the distance between the PTVTF polymer backbone chains, whereas the outer ring is mainly attributed to the mean intermolecular distance between the alkyl bristles of $PC_{70}BM$ moieties. In the presence of excess $PC_{70}BM$, the GIWAXS patterns showed new isotropic scattering rings at $2\theta_f = 8.4°$ (d-spacing = 0.94 nm), caused by scattering from the $PC_{70}BM$ domains (Figure 3e, f). The 33 and 50% fullerene blends showed broad weak scattering rings relative to the more vivid and sharp patterns of the blends with higher $PC_{70}BM$ content. This indicates that the blends with lower $PC_{70}BM$ content included more homogeneously blended PTVTF and $PC_{70}BM$ components with small domains, whereas the blends with higher $PC_{70}BM$ content formed phase-separated morphologies. Interestingly, the diffraction pattern resulting from the PTVTF polymer backbone chains was also influenced by the $PC_{70}BM$ -rich domains. The intensity of the inner scattering ring at $2\theta_f = 5.15°$, which corresponds to the interchain distance of the polymer backbone chains, was increased when excess quantities of $PC_{70}BM$ were used. In other words, the presence of $PC_{70}BM$ aggregates forced the polymers to aggregate with a regular range of interchain distances, despite the amorphous structural characteristics. For the detailed analysis, the integrated intensities of the scattering peaks at $2\theta_f = 5.15°$ normalized to the scattering peaks at 8.40° were determined by peak separation using Gaussian function and summarized in Table 1. As can be seen in Table 1, there is a certain trend that integrated peak intensity of PTVTF relative to $PC_{70}BM$ normalized by volume fraction of each component increases with more contents of $PC_{70}BM$ in the blend. Together with AFM, these results strongly support that PTVTF:$PC_{70}BM$ bulkheterojunction films have phase-separated morphology with excess contents of $PC_{70}BM$.

Table 1. Relative Integrated Intensities of Two Scattering Peaks at $2\theta_f$ = 5.15 and 8.40°[a]

	contents of $PC_{70}BM$			
	33%	50%	67%	80%
I (PTVTF)[b]/ I (PCBM)[c]	2.52	1.69	1.52	1.81
R, ratio[d]	1.1	1.5	2.73	6.39

[a]Here, to take change of volume fraction into account, the following relationships between integrated intensity and volume weres employed; (1) $I \propto VA$, (2) $R = (I_1/V_1)/(I_2/V_2)$, where the I is integral intensity, V is volume of scatterer, A is integrated intensity of unit volume, and R is relative integrated intensity between two peaks divided by unit volume. For the calculation of volume fraction, it was assumed that the densities of polymer PTVTF and $PC_{70}BM$ are similar to those of P3HT (1.15 g/mL) and $PC_{60}BM$(1.3 g/mL), respectively.[36] [b]Integrated intensity at $2\theta_f$ = 5.15° determined by peak separation using Gaussian function. [c]Integrated intensity at $2\theta_f$ = 8.40° determined by peak separation using Gaussian function. [d]Relative ratio of I(PTVTF) to I(PCBM) normalized by volume fraction of PTVTF in thin films.

To assess the effects of such phase separation on the charge transport characteristics of PTVTF/$PC_{70}BM$ blend films, we measured the hole and electron mobilities using the space charge limited (SCL) method, which describes J–V characteristics by $J \propto V^2$. The equation is known as Mott–Gurney equation[33]

$$J = \left(\frac{9}{8}\right)\varepsilon\varepsilon_0\mu\frac{(V^2)}{(d^3)}$$

where J is the current density, ε_0 is the permittivity of vacuum, ε is the relative permittivity of polymer that is assumed to be 3, μ is mobility, V is the voltage, and d is the thickness of the layer. Hole-only and electron-only devices were fabricated from the following structures: ITO/PEDOT:PSS/PTVTF: $PC_{70}BM$/Au for the hole-only device, and Al/PTVTF: $PC_{70}BM$/LiF/Al for the electron-only device. V_{BI} in the hole-only device was assumed as zero because the work functions of ITO/PEDOT:PSS and Au were similar. V_{BI} in the electron-only device was estimated from the difference in the work function between the Al and LiF/Al contacts as 0.3 V.[34] The experimental data were successfully fit given the constraint that the SCL equation can be applied only to the SCL region in which the slope of $\log(J) - \log(V)$ is 2 (Figure 4a, c). The obtained electron and hole mobilities of the PTVTF/$PC_{70}BM$ blend for all blend ratios are summarized in panels b and d in Figure 4, respectively. For both hole and electron charge carriers, fullerene content in excess of 67% produced higher mobilities than did more homogeneous blends with lower fullerene content, which is general observation.[35] It is noteworthy that both the electron and hole mobilities were enhanced by excess fullerene content, even though the blend films contained only very small quantities of hole conducting polymer, 25 or 33%. We propose that reordering of the polymer chain in the blends containing an excess of $PC_{70}BM$ enabled such hole mobility enhancement, as described in the GIWAS section.

Based on the general understanding of percolating pathways of the BHJ blend, we concluded that the PTVTF: $PC_{70}BM$ blend in dichlorobenzene with a fullerene content of 67% would be an ideal BHJ blend film for solar cell application. To correlate the observed morphology with the photovoltaic parameters, the J–V characteristics of these blends were measured under simulated solar illumination (Figure 5). As predicted from the relatively deep HOMO level in PTVTF, quite large V_{OC} values of 0.8–0.9 eV were observed in all blends. The PTVTF: $PC_{70}BM$ blend films showed photovoltaic performances that varied as a function of fullerene content. The fullerene content was optimal at 67%–80% with dichlorobenzene, which corresponds to fullerene fractions with optimal morphologies. As discussed earlier, a transition between homogeneous and phase-separated morphologies occurred between fullerene content of 50 and 67%. Across this transition, hole and electron mobilities, short circuit current, and power conversion efficiency (up to 3.1%) increased dramatically. The incident photon to current efficiency (IPCE) also followed this trend as a function of fullerene content, with a maximum IPCE of 44% for 67% fullerene (data not shown here).

Photodetector performances were measured using the same device consisting of PTVTF:DHFCBM and PTVTF:$PC_{70}BM$ with chopped monochromatic light (10 Hz). The AC photocurrent from the device was measured with a lock-in amplifier. Across the valid absorption range, responsivity, defined as the ratio of photocurrent to incident light power, was measured with a light intensity of 0.2 mW/cm^2 under forward bias (0.2 V). As indicated in Figure 6a, responsivity was enhanced as a result of phase separation throughout the range

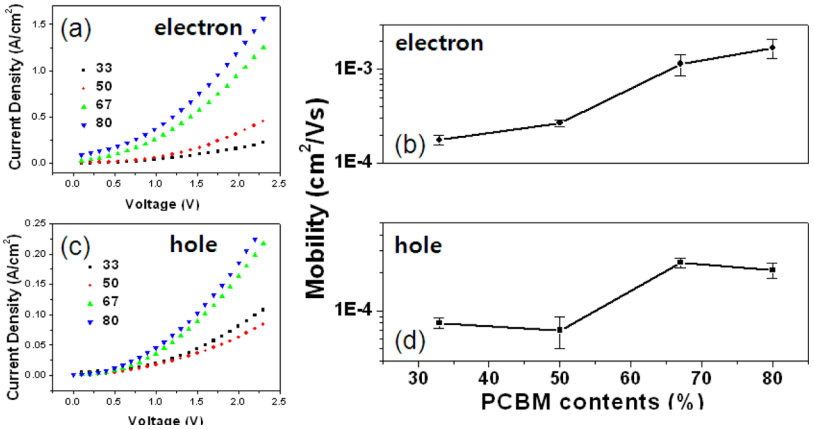

Figure 4. (a, c) J–V characteristics of PTVTF/[70]PCBM blend films fabricated as hole-only (or electron-only) devices. (b, d) The calculated mobilities are plotted as a function of fullerene content in the right panel.

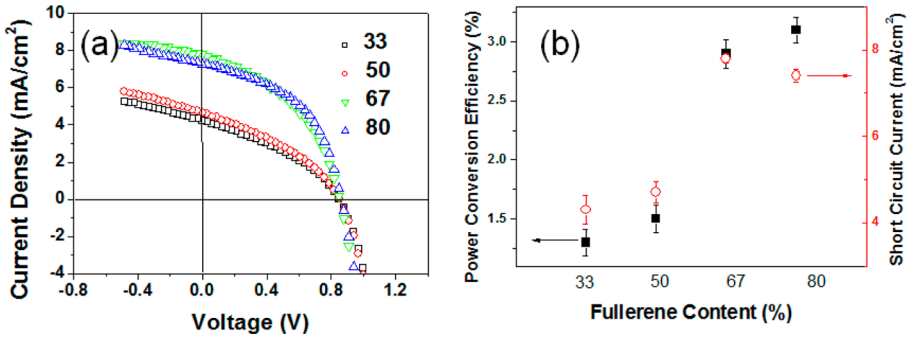

Figure 5. (a) Current density–voltage (J–V) characteristics of photovoltaic devices composed of PVTFT/PC70BM under 100 mW/cm^2 white light illumination. (b) Summary of measured power conversion efficiency and short circuit current.

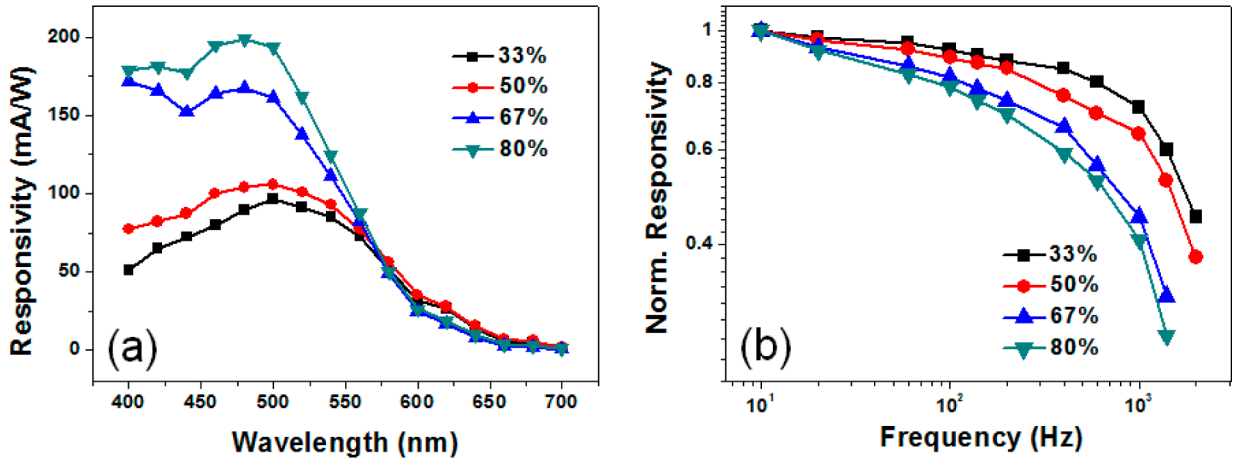

Figure 6. (a) Responsivity versus wavelength for PPDs with different PC70BM loading ratio. (b) Normalized responsivity versus chopping frequency to find 3-dB bandwidth for different PC70BM loading ratio.

of measured wavelength. The devices produced without phase separation showed a maximum responsivity of ~100 mA/W at 480 nm. When excess $PC_{70}BM$ was added and phase separation was achieved, the responsivity increased up to ~200 mA/W at 480 nm. This result is consistent with the PSC measurement, indicating that the phase separated morphology enabled more efficient charge extraction, possibly due to higher charge carrier mobility and/or longer photocarrier lifetime.

The responsivity of each device was subsequently measured as a function of modulation frequency to obtain 3 dB bandwidth which corresponds to the response time of our photodetectors. As shown in Figures 6b, the 3 dB bandwidth of the phase separated device is more than 2-fold shorter than that of the other devices. In addition, the former devices presented higher dark noise current than devices with lower $PC_{70}BM$ content. Considering the measured dark-noise current in each device ranging from 100 to 200 pAHz$^{-1/2}$ together with device geometry and bandwidth, the figure of merit of the photodetector, detectivity (D^*), was calculated and the results are summarized in Table 1. Despite increased responsivity as a result of phase separation, it is clearly shown that the detectors with excess content of PCBM resulted in lower D^* because of increased response time and noise current.

There are four major sources of noise current in photodetectors: thermal noise, shot noise, generation-recombination noise, and 1/f noise.[26] Among these, shot noise is related with both the photocurrent and dark current of devices. Therefore, higher charge carrier mobility of phase separated devices can be a possible source of the observed higher dark current of these

Table 2. Summary for Various Figure of Merits of Photodetectors: Responsivity, Bandwidth, Noise Current Density and Detectivity As a Function of $PC_{70}BM$ Loading Ratio

	responsivity (mA/W)	bandwidth (Hz)	noise current density (pA/Hz$^{1/2}$)	$D^* \times 10^9$ cmHz$^{1/2}$W^{1-})
33%	91	1060	51	11.1
50%	102	820	55	10.2
67%	154	240	89	5.2
80%	198	180	98	5.2

devices. Photodetector response time is closely related with photoconductive gain in devices where their geometry allows charge injection (i.e., forward bias). In these devices, photogenerated carriers can travel through the closed circuit by circulating several times depending on the charge carrier lifetime. The resulting photoconductive gain is consequently proportional to the charge carrier lifetime, and thus inversely proportional to the detector bandwidth. Although the photodetectors with homogeneous morphology have lower responsivity, their relatively lower noise current and higher bandwidth enabled a higher D^* compared to photodetectors with phase separated morphology. This result emphasizes the importance of developing an independent strategy for designing the photodetector separately from solar cell devices. Although it is not presently possible to suggest an unambiguous morphological protocol for optimizing photodetector performance, our results indicate that the performance of PPDs is also

strongly dependent upon the morphology, and the tendency can deviate from that observed in PSCs. It is believed that further study on the relationship between the morphology and performance of PPDs from various polymers can lead to the development of a clearer protocol for obtaining high performance PPDs.

CONCLUSION

Photoactive layers generated from blends of low crystalline polymeric semiconductors and $PC_{70}BM$ resulted in various BHJ morphologies according to the blend ratio. The blend films with excess contents of $PC_{70}BM$ revealed phase separated morphology with larger domain size of each component, which enabled higher hole−electron charge carrier mobility as well as higher power conversion efficiency as PSCs. The results further demonstrate that the longer charge carrier lifetime enabled by phase separated morphology, which is beneficial for PSCs performance and the responsivity of PPDs, can be disadvantageous for fast response of PPDs. Through optimized morphology which has balanced response time and photocurrent, we demonstrated high performance PPDs with D^* on the order of 1×10^{10} cm $Hz^{1/2}$ W^{-1}. These results show the importance of developing an independent strategy for designing PPDs separately from PSCs.

AUTHOR INFORMATION

Corresponding Author

*E-mail: dchung@dau.ac.kr (D.S.C.), ree@postech.edu (M.R.), ykim@gnu.ac.kr (Y.-H.K.).

Notes

The authors declare no competing financial interest.

ACKNOWLEDGMENTS

This research was supported by Ministry of Knowledge Economy of Korean government and Basic Research Program through the National Foundation of Korea by the Ministry of Education, Science and Technology (2011-0027499) and (2011-000310).

REFERENCES

(1) Sariciftci, N. S.; Smilowitz, L.; Heeger, A. J.; Wudl, F. *Science* **1992**, *258*, 1474.
(2) Yu, G.; Gao, J.; Hummelen, J. C.; Wudl, F.; Heeger, A. J. *Science* **1995**, *270*, 1789.
(3) Chen, H. -Y.; Hou, J.; Zhang, S.; Liang, Y.; Yang, G.; Yang, Y.; Yu, L.; Wu, Y.; Li, G. *Nat. Photon.* **2009**, *3*, 649.
(4) Cheng, Y.-J.; Yang, S.-H.; Hsu, C.-S. *Chem. Rev.* **2009**, *109*, 5868.
(5) (a) Chen, M.-H.; Hou, J.; Hong, Z.; Yang, G.; Sista, S.; Chen, L.-M.; Yang, Y. *Adv. Mater.* **2009**, *21*, 4238. (b) Li, G.; Shrotriya, V.; Huang, J.; Yao, Y.; Moriarty, T.; Emery, K.; Yang, Y. *Nat. Mater.* **2005**, *4*, 864.
(6) Mayer, A. C.; Toney, M. F.; Scully, S. R.; Rivnay, J.; Brabec, C. J.; Scharber, M.; Koppe, M.; Heeney, M.; McCulloch, I; McGehee, M. D. *Adv. Funct. Mater.* **2009**, *19*, 1173.
(7) Woo, C. H.; Thompson, B. C.; Kim, B. J.; Toney, M. F.; Fréchet, J. M. J. *J. Am. Chem. Soc.* **2008**, *130*, 16324.
(8) Chung, D. S.; Park, J. W.; Kim, S.-O.; Heo, K.; Park, C. E.; Ree, M.; Kim, Y.-H.; Kwon, S.-K. *Chem. Mater.* **2009**, *21*, 5499.
(9) Piliego, C.; T. Holcombe, W.; Douglas, J. D.; Woo, C. H.; Beaujuge, P. M.; Frechet, J. M. J. *J. Am. Chem. Soc.* **2010**, *132*, 7595.
(10) Xiao, S.; Stuart, A. C.; Liu, S.; Zhou, H.; You, W. *Adv. Func. Mater.* **2010**, *20*, 635.
(11) Gunes, S.; Neugebauer, H.; Sariciftci, N. S. *Chem. Rev.* **2007**, *107*, 1324.
(12) Thompson, B. C.; Fréchet, J. M. J. *Angew. Chem., Int. Ed.* **2008**, *47*, 58.
(13) Li, G.; Shrotriya, V.; Huang, J. S.; Yao, Y.; Moriarty, T.; Emery, K.; Yang, Y. *Nat. Mater.* **2005**, *4*, 864.
(14) Wienk, M. M.; Turbiez, M.; Gilot, J.; Janssen, R. A. J. *Adv. Mater.* **2008**, *20*, 2556.
(15) Zhang, F.; Jespersen, K. G.; Björström, C.; Svensson, M.; Andersson, M. R.; Sundström, V.; Magnusson, K.; Moons, E.; Yartsev, A.; Inganäs, O. *Adv. Funct. Mater.* **2006**, *16*, 667.
(16) Zhou, H.; Yang, L.; You, W. *Macromolecules* **2012**, *45*, 607.
(17) Beaujuge, P. M.; Fréchet, J. M. J. *J. Am. Chem. Soc.* **2011**, *133*, 20009.
(18) Facchetti, A. *Chem. Mater.* **2011**, *23*, 733.
(19) Dennler, G.; Scharber, M. C.; Brabec, C. J. *Adv. Mater.* **2009**, *21*, 1323.
(20) Chang, E. C.; Chao, C.-I.; Lee, R.-H. *J. Appl. Polym. Sci.* **2006**, *101*, 1919.
(21) Yu, G.; Pakbaz, K.; Heeger, A. J. *Appl. Phys. Lett.* **1994**, *64*, 3422.
(22) (a) Ma, W.; Yang, C.; Gong, X.; Lee, K.; Heeger, A. J. *Adv. Func. Mater.* **2005**, *15*, 1617. (b) Irwin, M. D.; Buchholz, D. B.; Hains, A. W.; Chang, R. P. H.; Marks, T. J. *Proc. Natl. Acad. Sci. U.S.A.* **2008**, *105*, 2783. (c) Kim, J. Y.; Kim, S. H.; Lee, H.-Ho; Lee, K.; Ma, W.; Gong, X.; Heeger, A. J. *Adv. Mater.* **2006**, *18*, 572.
(23) Chen, H. Y.; Lo, M. K. F.; Yang, G.; Monbouquette, H. G.; Yang, Y. *Nat. Nanotechnol.* **2008**, *3*, 543.
(24) Peet, J.; Kim, J. Y.; Coates, N. E.; Ma, W. L.; Moses, D.; Heeger, A. J.; Bazan, G. C. *Nat. Mater.* **2007**, *6*, 497 2.
(25) Gong, X.; Tong, M. H.; Xia, Y. J.; Cai, W. Z.; Moon, J. S.; Cao, Y.; Yu, G.; Shieh, C. L.; Nilsson, B.; Heeger, A. J. *Science* **2009**, *325*, 1665.
(26) (a) Scharber, M. C.; Mühlbacher, D.; Koppe, M.; Denk, P.; Waldauf, C.; Heeger, A. J.; Brabec, C. J. *Adv. Mater.* **2006**, *18*, 789. (b) Tvingstedt, T.; Vandewal, K.; Gadisa, A.; Zhang, F.; Manca, J.; Inganäs, O. *J. Am. Chem. Soc.* **2009**, *131*, 11819. (c) Blakesley, J. C.; Neher, D. *Phys. Rev. B* **2011**, *84*, 075210.
(27) Konstantatos, G.; Howard, I.; Fischer, A.; Hoogland, S.; Clifford, J.; Klem, E.; Levina, L.; Sargent, E. H. *Nature* **2006**, *442*, 180.
(28) Konstantatos, G.; Clifford, J.; Levina, L.; Sargent, E. H. *Nat. Photon.* **2007**, *1*, 531.
(29) Clifford, J.; Konstantatos, G.; Hoogland, S.; Levina, L.; Sargent, E. H. *Nature Nanotechnol.* **2009**, *4*, 40.
(30) Clifford, J.; Johnston, K. W.; Levina, L.; Sargent, E. H. *Appl. Phys. Lett.* **2007**, *91*, 253.
(31) Chung, D. S.; Lee, S. J.; Park, J. W.; Choi, D. B.; Lee, D. H.; Park, J. W.; Shin, S. C.; Kim, Y. H.; Kwon, S.-K.; Park, C. E. *Chem. Mater.* **2008**, *20*, 3450. (b) Chung, D. S.; Lee, D. H.; Yang, C.; Hong, K.; Park, C. E.; Park, J. W.; Kwon, S.-K. *Appl. Phys, Lett.* **2008**, *93*, 033303.
(32) (a) Lee, B.; Park, Y.-H.; Hwang, Y.-T.; Oh, W.; Yoon, J.; Ree, M. *Nat. Mater.* **2005**, *4*, 147. (b) Heo, K.; Yoon, J.; Jin, S.; Kim, J.; Kim, K.-W.; Shin, T. J.; Chung, B.; Chang, T.; Ree, M. *J. Appl. Crystallogr.* **2008**, *41*, 281. (c) Yoon, J.; Kim, K.-W.; Kim, J.; Heo, K.; Jin, K. S.; Jin, S.; Shin, T. J.; Lee, B.; Rho, Y.; Ahn, B.; Ree, M. *Macromol. Res.* **2008**, *16*, 575.
(33) (a) Mott, N. F.; Gurney, R. W. *Electonic Processes in Ionic Crystals*; Dover: New York, 1964. (b) Martens, H. C. F.; Blom, P. W. M.; Schoo, H. F. M. *Phys. Rev. B* **2000**, *61*, 7489.
(34) Brown, T. M.; Friend, R. H.; Millard, I. S.; Lacey, D. J.; Burroughes, J. H. *Appl. Phys. Lett.* **2000**, *77*, 3096.
(35) (a) Moon, J. S.; Takacs, C. J.; Cho, S.; Coffin, R. C.; Kim, H.; Bazan, G. C.; Heeger, A. J. *Nano Lett.* **2010**, *10*, 4005. (b) Chen, M.-C.; Liaw, D.-J.; Chen, W.-H.; Huang, Y.-C.; Sharma, J.; Tai, Y. *Appl. Phys. Lett.* **2011**, *99*, 223305.
(36) Treat, N. D.; Brady, M. A.; Smith, G.; Toney, M. F.; Kramer, E. J.; Hawker, C. J.; Chabinyc, M. L. *Adv. Energy Mater.* **2011**, *1*, 82.